Supplementary Information

Flexoelectric Polarization–Electric Field Coupling-Driven Phase Transformation in Epitaxial Films

Seong Min Park[a], WooJun Seol[a], Su Yong Lee[b], Hyunjin Joh[a], Keeyong Lee[c], Sang Ho Oh[c], Hyeon Jun Lee[*d], and Ji Young Jo[*a]

[a]Department of Materials Science and Engineering, Gwangju Institute of Science and Technology; Gwangju, 61005, South Korea.

[b]Pohang Accelerator Laboratory, Pohang University of Science and Technology; Pohang, 37673, South Korea.

[c]Department of Energy Engineering, Korea Institute of Energy Technology (KENTECH); Naju, 58330, South Korea.

[d]Department of Materials Science and Engineering, Kangwon National University; Samcheok, 25913, South Korea.

*Corresponding author. E-mail: jyjo@gist.ac.kr, hjlee.mse@kangwon.ac.kr

Estimation of lattice parameters of BF-BT thin film using XRD

Reciprocal space maps (RSMs) in Fig. 1c and d were reconstructed from the captured scattering X-ray as a function of Q_y-Q_z and Q_x-Q_z around (002) and (-103), respectively, to estimate lattice parameters of the BF-BT thin film. In this context, Q_x and Q_y represent scattering wave vectors along the in-plane [100] and [010] direction, while Q_z denotes the wave vector along the out-of-plane [001] direction. Based on the interplanar spacing comparisons with the previous research on BF-BT films[S1], we found that two distinct diffraction peaks arising from the rhombohedral (R-phase) and tetragonal (T-phase) of the BF-BT thin film appear at $Q_z = 3.082$ Å^{-1} and 2.910 Å^{-1} (where $Q_y = 0$). The T-phase produces a (-103) reflection at Q_x value of 1.608 Å^{-1}, identical to that of the substrate, while that of the R-phase exhibits a diffusive scattering intensity along the in-plane direction with Q_x maxima at 1.562 Å^{-1}. These indicate that the T-phase is coherently strained with the estimated *a*- and *c*-axis lattice parameters of 3.907 Å and 4.318 Å (*c*/*a* ratio of 1.11). In contrast, the R-phase is fully relaxed with that of 4.022 Å and 4.077 Å (*c*/*a* ratio of 1.01). For the flexoelectric layer, the gradual layer-by-layer lattice distribution contributes to overall background intensity; however, significant thermal scattering from SRO and STO makes the flexoelectric layer reflection difficult to identify in reciprocal space.

Effect of phase transformation in flexoelectric layer on x-ray diffraction profiles

Kinematic simulation was conducted to evaluate the effect of phase transformation within the flexoelectric layer on x-ray diffraction (XRD) profiles. The total film thickness was kept constant, assuming that the phase transformation is spatially confined to the flexoelectric layer, as illustrated in Fig. S5.

Fig. S6a and b show the simulated (002) XRD profiles corresponding to gradual phase transformation of the flexoelectric layer into either T-phase ($^{\Delta t_{T-phase}}$) and R-phase ($\Delta t_{R-phase}$), respectively. These profiles exhibit intricate interference fringes that arise from the collective structural contributions of T-phase, R-phase, and flexoelectric layer, whose individual thickness and lattice parameter generate overlapped diffraction pattern. The interference fringes originating from R-phase are not observed in experimental data due to the disorder of crystallographic orientation along the out-of-plane direction in R-phase layer.

The phase transformation in the flexoelectric layer results in a redistribution of the calculated diffraction intensity, which is an evident in both the fringe spacing and the scattered intensity. Based on the reciprocal relationship between layer thickness and Bragg-fringe spacing, our simulation shows that transformation of the flexoelectric layer into T-phase leads to a decrease in Bragg-fringe spacing, while transformation into the R-phase results in increased spacing. The phase transformation also changes the normalized peak intensity: when the flexoelectric layer transforms into the T-phase, the normalized intensity of the T-phase increases while that of the R-phase slightly decreases (Fig. S6c). Conversely, transformation into the R-phase leads to an increase in R-phase intensity and a reduction in T-phase intensity (Fig. S6d). These simulation results indicate that even modest changes in the thickness of the flexoelectric layer can significantly affect the overall XRD profiles.

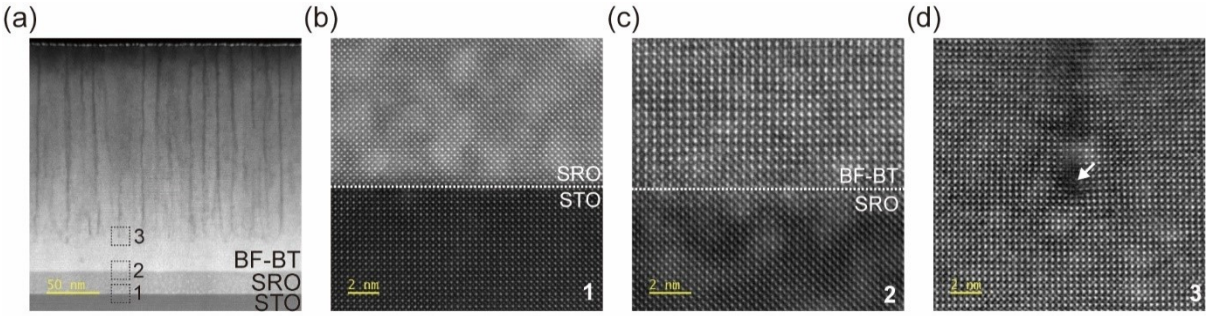

Fig. S1. Cross-sectional STEM analysis of epitaxial BF-BT thin film.

(a) Low magnitude STEM images including BF-BT thin film, $SrRuO_3$ (SRO) bottom electrode, and $SrTiO_3$ substrate. The black dot square boxes indicate the selected region of interest for high magnitude STEM images. (b) The high magnitude STEM images near the interfaces between SRO film and STO substrate (**region 1**), (c) between BF-BT and SRO films (**region 2**), and (d) between tetragonal phase (T-phase) and flexoelectric layer (**region 3**). The white arrow indicates misfit dislocation that appears to reduce the elastic strain induced by the lattice mismatch between the BF-BT thin film and STO substrate, which is evidence of the strain relaxation.[S2]

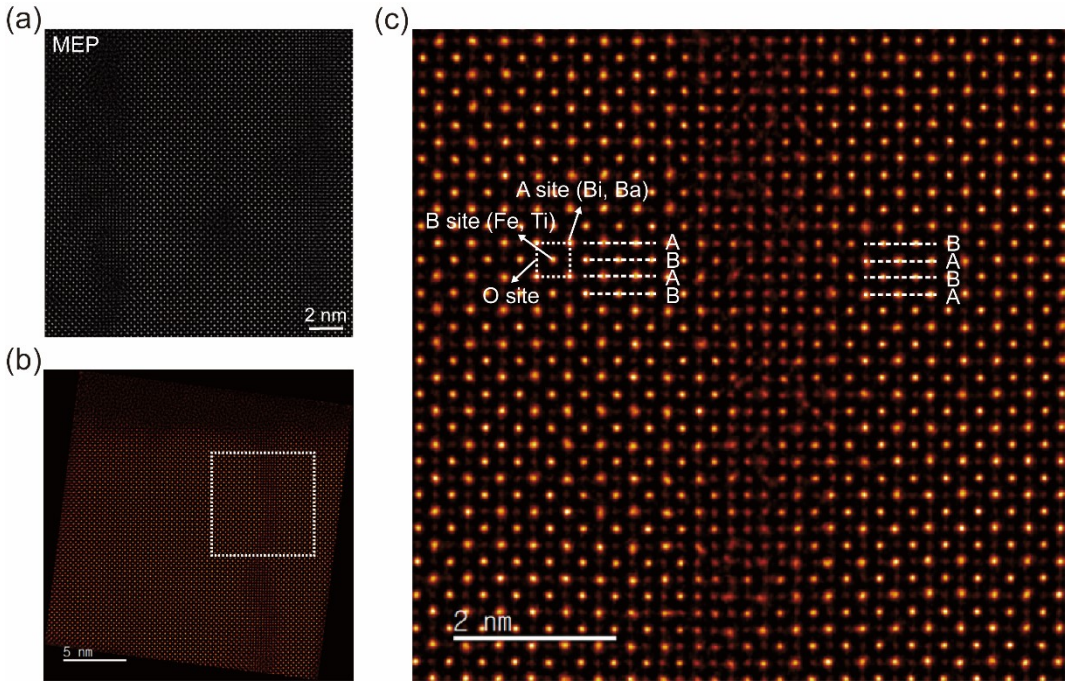

Fig. S2. Cross-sectional MEP analysis of epitaxial BF-BT thin film.
(a) Cross-sectional MEP image of the BF-BT R-phase layer. (b) Low and (c) high magnitude of atomic-mapping images near the straight-line defect in the BF-BT layer.

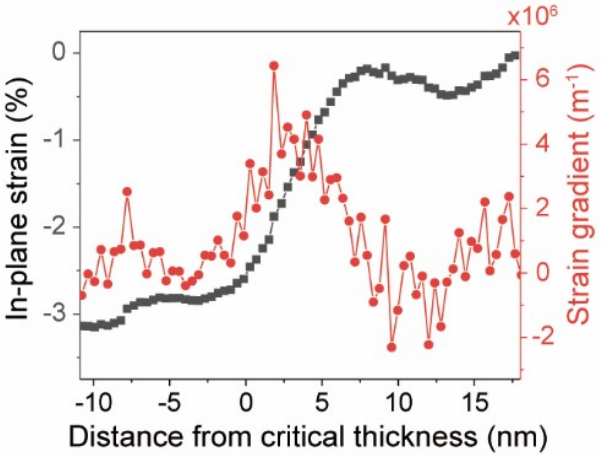

Fig. S3. Estimation of in-plane strain gradient.

In-plane strain and corresponding strain gradient ($\partial u_{yy}/\partial t$) of BF-BT thin film along the out-of-plane [001] direction is estimated using intensity variation of line profile of the STEM image in Fig. 1b. The strain gradient of approximately 4×10^6 m^{-1} is generated by a gradual relaxation of in-plane strain from -3.15% up to 0% within the flexoelectric layer with a relaxation length of 6 nm above the critical thickness.

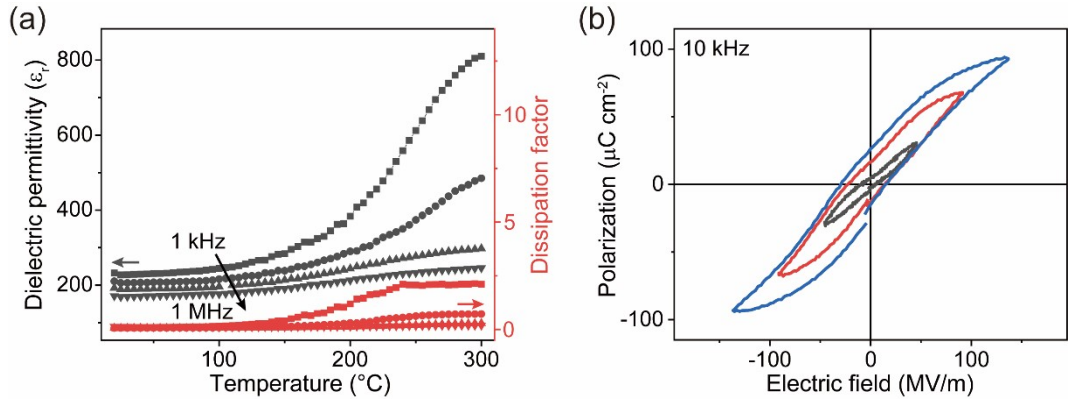

Fig. S4. Relaxor-like behavior of BF-BT thin film.

(a) Dielectric permittivity (left, black) and dissipation factor (right, red) as a function of temperature (20-300°C) and frequency (1-1000 kHz). (b) Polarization–electric field hysteresis loops measured at a frequency of 10 kHz at room-temperature.

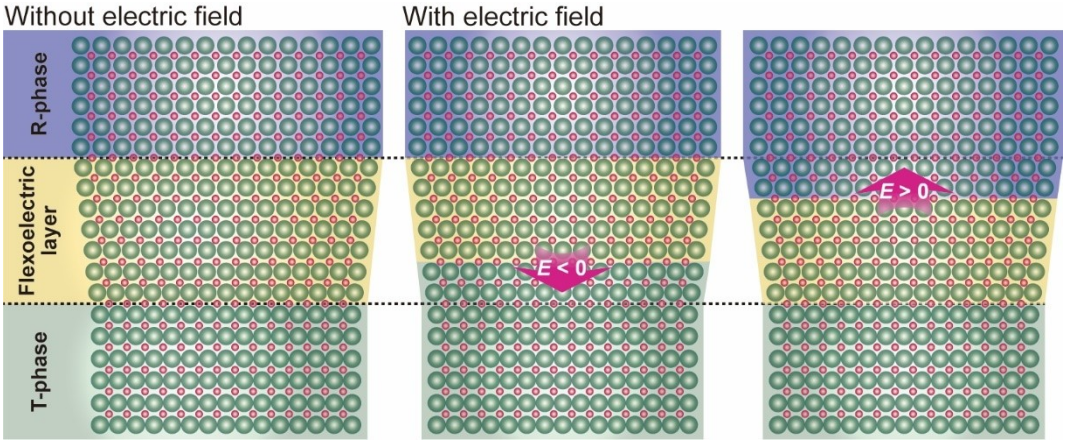

Fig. S5. Hypothesized phase transformation for kinematic simulation.
Schematic illustration of phase transformation confined to the flexoelectric layer. The black dot lines indicate the interfaces of the flexoelectric layer.

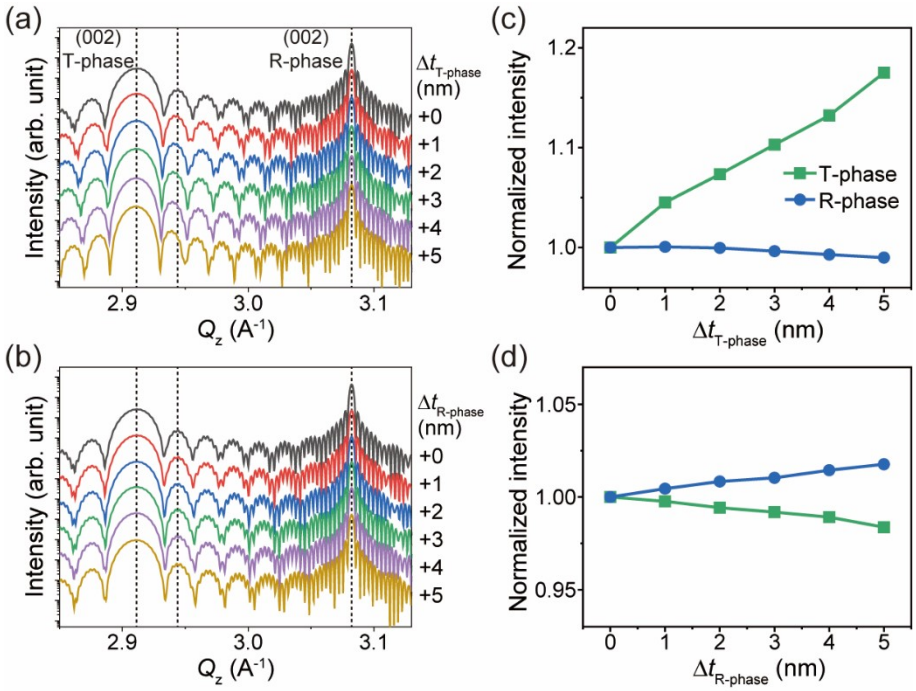

Fig. S6. Thickness-dependent XRD simulation of phase transformation in flexoelectric layer.

(a) Simulated (002) XRD profiles from BF-BT thin film computed with varying thickness $^{\Delta t_{T-phase}}$= 0, 1, 2, 3, 4, 5 nm and (b) $^{\Delta t_{R-phase}}$= 0, 1, 2, 3, 4, 5 nm. (c) Normalized intensity of the R- and T-phases corresponding to $^{\Delta t_{T-phase}}$ and (d) $^{\Delta t_{R-phase}}$.

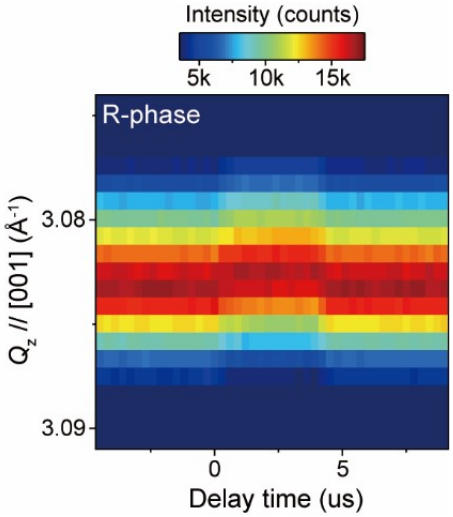

Fig. S7. Time dependence of intensity distribution of (002) Bragg reflection of R-phase under electric field of 28 MV m^{-1} for 4 μs.

The time constants associated with the response to applied electric field can be determined by using piezoelectric shift of the Bragg reflection. The intensity maximum of R-phase shifts over approximately 700 ns during and after the applied electric field, indicating that the charging and discharging time constants of the BF-BT capacitor are less than 700 ns. Thus, the time interval, defined as 3 μs from the beginning of the electric pulse, is sufficient for the detection of electric field dependent XRD profiles to avoid charging and discharging effects of the capacitor.

Table S1.
Comparison of ferroelectric and piezoelectric properties of T-phase of BF-BT thin film in this study with purely tetragonal phase of $Pb(Zr,Ti)O_3$, $BaTiO_3$, $BiFeO_3$, and $BiFeO_3$-$BaTiO_3$ thin films system.

Materials	Thickness (nm)	d_{33} (pm V^{-1})	P_r (μC cm^{-2})	ε_r	$P_r\varepsilon_r$	Ref.
$Pb(Zr_{0.2}Ti_{0.8})O_3$	30	45	105	90	9450	(S3)
$BaTiO_3$	80	21	/	/	/	(S4)
$BiFeO_3$	20	30	/	/	/	(S5)
$BiFeO_3$	15	/	150	/	/	(S6)
$BiFeO_3$	30	/	/	16	/	(S7)
$0.68BiFeO_3$-$0.32BaTiO_3$	300	35	87	74	6438	(S1)
$0.67BiFeO_3$-$0.33BaTiO_3$	23	351	29	371	10759	This work

Table S2.
Atomic scattering factors of Bi, Fe, Ba, Ti, and O.

Atom	$f^0_j + f'_j$	f''_j
Bi	78.3690	6.53426
Fe	25.9946	2.23854
Ba	56.0548	6.24546
Ti	22.3908	1.26095
O	8.03533	0.02075

Table S3.
Fractional atomic position based on crystal structures.

	atom	Fractional atomic position			Ref.
		u	v	w	
$BiFeO_3$ (*P4mm*)	Bi	0	0	0	(S8)
	Fe	0.5	0.5	0.439	
	O1	0.5	0.5	-0.17	
	O2	0	0.5	0.294	
	O3	0.5	0	0.294	
$BiFeO_3$ (*R3C*)	Bi	0	0	0	(S9)
	Fe	0	0	0.22056	
	O	0.44050	0.01711	0.95214	
$BaTiO_3$ (*P4mm*)	Ba	0	0	0	(S10)
	Ti	0.5	0.5	0.5224	
	O1	0.5	0.5	0.9756	
	O2	0.5	0	0.4895	

References

S1 Y.-Q. Hu, N.-T. Liu, J. Lao, R.-H. Liang, X. Deng, Z. Guan, B.-B. Chen, H. Peng, N. Zhong, P-H. Xiang, & C.-G. Duan, *ACS Appl. Mater. Interfaces*, 2022, **14**, 36825-36833.

S2 D. J. Dunstan, *J. Mater. Sci.: Mater. Electron*, 1997, **8**, 337-375.

S3 I. Vrejoiu, G. Le Rhun, L. Pintilie, D. Hesse, M. Alexe, & U. Gösele, *Advanced Materials*, 2006, **18**, 1657-1661.

S4 K. P. Kelley, D. E. Yilmaz, L. Collins, Y. Sharma, H. N. Lee, D. Akbarian, A. C. T. van Duin, P. Ganesh, & R. K. Vasudevan, *Phys. Rev. Mater.*, 2020, **4**, 024407.

S5 J. X. Zhang, B. Xiang, O. He, J. Seidel, R. J. Zeches, P. Yu, S. Y. Yang, C. H. Wang, Y-H. Chu, L. W. Martin, A. M. Minor, & R. Ramesh, *Nat. Nanotechnol.*, 2011, **6**, 98-102.

S6 J. X. Zhang, Q. He, M. Trassin, W. Luo, D. Yi, M. D. Rossell, P. Yu, L. You, & C. H. Wang, *Phys. Rev. Lett.*, 2011, **107**, 147602.

S7 J. Zhu, Z. Yin, Z. Fu, Y. Zhao, X. Zhang, X. Liu, J. You, X. Li, J. Meng, H. Liu, & J. Wu, *J. Cryst. Growth*, 2017, **459**, 178-184.

S8 L. Yin, W. Mi, & X. Wang, *Sci. Rep.*, 2016, **6**, 20591.

S9 J. Du, A. E. Phillips, D. C. Arnold, D. A. Keen, M. G. Tucker, & M. T. Dove, *Phys. Rev. B*, 2019, **100**, 104111.

S10 G. H. Kwei, A. C. Lawson, S. J. L. Billinge, & S. W. Cheong, *J. Phys. Chem.*, 1993, **97**, 2368-2377.